Talanta 276 (2024) 126272

Contents lists available at ScienceDirect

Talanta

journal homepage: www.elsevier.com/locate/talanta

Highly sensitive photoelectrochemical biosensing detection of early cardiac injury enabled by novel self-assembled $Bi_2O_3/MgIn_2S_4$ photoelectrode coupled with $ZnSnO_3$ quencher

Haiyang Gao [a], Xuan Kuang [a], Bing An [a], Jinjie Liu [a], Kun Xu [a], Hongmin Ma [a], Dongquan Leng [a,**], Xuejing Liu [a,***], Qin Wei [a,b,*], Huangxian Ju [a,c]

[a] Collaborative Innovation Center for Green Chemical Manufacturing and Accurate Detection, Key Laboratory of Interfacial Reaction & Sensing Analysis in Universities of Shandong, School of Chemistry and Chemical Engineering, University of Jinan, Jinan, 250022, PR China
[b] Department of Chemistry, Sungkyunkwan University, Suwon, 16419, Republic of Korea
[c] State Key Laboratory of Analytical Chemistry for Life Science, Department of Chemistry, Nanjing University, Nanjing, 210023, PR China

ARTICLE INFO

Keywords:
$Bi_2O_3/MgIn_2S_4$
$ZnSnO_3$
Quencher
Photoelectrochemical biosensor
H-FABP

ABSTRACT

The development of photoelectrochemical (PEC) biosensors plays a critical role in enabling timely intervention and personalized treatment for cardiac injury. Herein, a novel approach is presented for the fabrication of highly sensitive PEC biosensor employing $Bi_2O_3/MgIn_2S_4$ heterojunction for the ultrasensitive detection of heart fatty acid binding protein (H-FABP). The $Bi_2O_3/MgIn_2S_4$ heterojunction, synthesized through in-situ growth of $MgIn_2S_4$ on Bi_2O_3 nanoplates, offers superior attributes including a larger specific surface area and more homogeneous distribution, leading to enhanced sensing sensitivity. The well-matched valence and conduction bands of Bi_2O_3 and $MgIn_2S_4$ effectively suppress the recombination of photogenerated carriers and facilitate electron transfer, resulting in a significantly improved photocurrent signal response. And the presence of the secondary antibody marker ($ZnSnO_3$) introduces steric hindrance that hinders electron transfer between ascorbic acid and the photoelectrode, leading to a reduction in photocurrent signal. Additionally, the competition between the $ZnSnO_3$ marker and the $Bi_2O_3/MgIn_2S_4$ heterojunction material for the excitation light source further diminishes the photocurrent signal response. After rigorous repeatability and selectivity tests, the PEC biosensor exhibited excellent performance, and the linear detection range of the biosensor was determined to be 0.05 pg/mL to 100 ng/mL with a remarkable detection limit of 0.029 pg/mL (S/N = 3).

1. Introduction

Photoelectrochemical (PEC) technology, with its ability to convert optical signals into electrical signals [1–3], has garnered significant global attention [4,5] due to its exceptional properties including low background interference [6,7], high sensitivity [8], and seamless integration with diverse detection modes [9,10]. These remarkable attributes have propelled PEC to the forefront of international research and paved the way for its widespread adoption in various fields [11,12]. However, single electrode materials usually have the defect of the lower photocurrent signal response [13] due to the quick recombination of the photogenerated carrier [14] and the slow rate of electron transfer [15]. Moreover, during the photocurrent signal testing process, the weak response of the biosensor photocurrent signal and poor stability [16,17] due to the photoelectrode material detachment [18] are also obstacles to the development of photoelectrochemical sensors. Therefore, there is an urgent need to find new high-performance photoelectrode materials [19] and more sensitive and effective detection methods [20] and modes for the detection of disease markers [21].

Bismuth oxide (Bi_2O_3) is a narrow band gap n-type semiconductor material with excellent performance [22–24], with a band gap between 2.1 and 2.85 eV [25]. It has promising applications in the photoelectrochemical field, but the photoelectric conversion efficiency of single Bi_2O_3 material is lower [26,27]. Therefore, it must be improved

* Corresponding author.
** Corresponding author.
*** Corresponding author.
E-mail addresses: wlkqldq@163.com (D. Leng), chm_liuxj@ujn.edu.cn (X. Liu), sdjndxwq@163.com (Q. Wei).

https://doi.org/10.1016/j.talanta.2024.126272
Received 25 January 2024; Received in revised form 9 May 2024; Accepted 15 May 2024
Available online 21 May 2024

by constructing semiconductor heterostructures, metal ion doping, surface sensitization and other methods. For example, Wang et al. prepared a highly sensitive photoelectrochemical biosensor [28] based on Bi_2O_3@Bi_2S_3 heterojunction for the detection of L-cysteine, which exhibited excellent photoelectric performance. The photocurrent signal is three times higher than the single Bi_2O_3 electrode material, which is mainly attributed to the suitable bandgap position of Bi_2O_3 and Bi_2S_3 and the formation of the p-n heterostructure. In addition to the above systems, Bi_2O_3 materials can also form heterojunctions with other semiconductor materials such as TiO_2 [27], WO_3 [29], and g-C_3N_4 [30] and so on, which shows that Bi_2O_3 fulfils a key role in the terms of photoelectrochemical biosensing and has promising research prospects. $MgIn_2S_4$ is a type of ternary sulfur compound with excellent optical, electrical, and mechanical properties [31], widely used in fields such as photoelectrochemical sensing, photocatalysis, and photodegradation [32]. Besides, $MgIn_2S_4$ has a suitable band gap [33], and the positions of the valence and conduction bands can be perfectly matched with those of Bi_2O_3, which effectively makes up for the shortcomings of the single-electrode materials of Bi_2O_3 and $MgIn_2S_4$ after forming the semiconductor heterojunction. Zinc stannate ($ZnSnO_3$), as a multifunctional material, has potential applications [34] in photoelectric catalysis, photoelectrochemical biosensing, gas sensing and other fields. $ZnSnO_3$ has a wider band gap [35], resulting in a weaker ability to absorb visible light. As a result, the steric hindrance and the ability to absorb light of $ZnSnO_3$ can result in a significant decrease in photocurrent signal.

On the basis of various quenching strategies and methods, such as the steric hindrance effect [36], PEC biosensors have a wide range of development prospects [37]. The performance of the material used for the photoelectric electrode and signal amplification strategy are the keys to the quenching PEC biosensor. Meng et al. used the ZIF-8 polyhedron embedded with the prepared graphene quantum dots (GQDs@ZIF-8 polyhedron) as an efficient quencher [38] for PEC signal, which inhibited the photocurrent signal response of the photoelectrode [39,40] through the steric effect and precipitation reaction [41,42]. In this study, a new high-performance semiconductor heterojunction material was synthesized by in-situ growth of substrate material on the surface of the photoelectrode, and applied to the PEC biosensor. Simultaneously, a novel PEC biosensor was constructed using the quenching strategy based on steric hindrance effect. In addition, the in-situ growth method has better stability and reliability than the dropwise addition of electrode materials to the surface of the photoelectrode, which overcomes the problem that electrode materials are prone to detachment during the test process. The work combines in-situ growth with quenching strategy based on steric hindrance effects, which leads to improve sensitivity of the biosensor greatly and is significant for pathology detection and physiological monitoring.

In this work, $Bi_2O_3/MgIn_2S_4$ heterojunction material was innovatively prepared on the surface of photoelectrode using in-situ synthesis, and on the other hand, a quenching strategy based on the steric hindrance effect was used to fabricate a photoelectrochemical biosensor for the detection of biomarkers. The prepared FTO/Bi_2O_3 photoelectrode has the strong points of large specific surface area and uniform distribution. Additionally, $MgIn_2S_4$ material was also prepared on the substrate using in-situ synthesis, and the photocurrent signal of the synthesized heterojunction material was greatly improved, fully demonstrating the excellent performance of the $Bi_2O_3/MgIn_2S_4$ heterojunction material. As the photoelectrode was modified layer by layer, the steric hindrance gradually increased, affecting the electron transfer rate and causing its photocurrent signal to continuously decrease. In addition, the competition between the secondary antibody marker ($ZnSnO_3$) and heterojunction material for excitation light source further reduces the photocurrent signal response. Due to the double quenching effect, the photocurrent signal response of photoelectrochemical biosensors is greatly reduced. However, because of the high initial photocurrent response, the sensitivity and accuracy of biosensor detection are higher compared to other sensors.

2. Experimental section

2.1. Experimental equipment and reagents

The particulars of the experiment can be found in the Supporting *Information* such as equipment and reagents.

2.2. Preparation of Bi_2O_3

Bi_2O_3 was synthetized on the basis of the previously reported method [18]. Firstly, 0.97 g of $Bi(NO_3)_3{\cdot}5H_2O$ was dissolved in 20 mL of ultrapure water, and then 1 mL of triethanolamine was added with stirring for 15 min. Then KOH (7.14 mol L^{-1}) was added drop by drop until the above solution became clear. Then the solution was poured into a 100 mL reactor, and FTO glass sheet measuring 4 cm by 2 cm was dipped diagonally into the solution with the conductive side facing upwards and reacted for 2 h at 65 °C. The FTO glass sheet obtained was rinsed in ultrapure water and dried, and calcined at 320 °C in the air at a heat rate of 5 °C·min^{-1} for 60 min. The Bi_2O_3-modified FTO glass sheet was prepared after the temperature dropped to room temperature.

2.3. Preparation of $Bi_2O_3/MgIn_2S_4$

$Bi_2O_3/MgIn_2S_4$ heterojunction was synthesized by hydrothermal method [13]. 0.1538 g of $Mg(NO_3)_2{\cdot}6H_2O$ and 0.3609 g of In $(NO_3)_3{\cdot}5H_2O$ were dissolved in 20 mL of ultrapure water and stirred for 30 min. Then, 0.2909 g of L-cysteine was added to the above solution, followed by stirring for another 20 min. The solution was transferred to a 100 mL reactor, and then the above synthesized Bi_2O_3-modified FTO glass plate was dipped diagonally into the solution with the conductive side facing downward, and the reaction was carried out for 12 h at 160 °C. After the temperature was cooled to room temperature, the modified FTO glass sheet was collected and rinsed with ultrapure water and finally dried.

2.4. Synthesis of ammoniated $ZnSnO_3$ and $ZnSnO_3/Ab_2$

0.16 g of $SnCl_4{\cdot}5H_2O$ and 0.07 g of NaOH were dissolved in the 20 mL of ultrapure water while stirring, after which the pH of the solution was adjusted to 12.2 by adding 3 mol L^{-1} NaOH dropwise. Under stirring at 95 °C, 0.13 g of $ZnSO_4{\cdot}7H_2O$ was quickly added and then stirred for another 5 min until the mixture was stirred homogeneously, which was aged for 12 h at 95 °C. After cooling and centrifugation, the gained precipitate was vacuum dried at 60 °C for more than 10 h. The precipitate was calcined at 580 °C for 2 h at a heating rate of 5 °C·min^{-1} to obtain $ZnSnO_3$ [43].

$ZnSnO_3$ (20 mg) was dispersed in anhydrous ethanol (10 mL) containing APTES (0.15 mL), which was stirred at 70 °C for 1.5 h. After rinsing and drying, the synthesis of ammoniated $ZnSnO_3$ was completed.

Firstly, 6 mg of ammoniated $ZnSnO_3$ was dissolved in 1.5 mL of ultrapure water, followed by the addition of 60 μL (2.5 % wt) of glutaraldehyde, which was oscillated for 4 h. Rinsing with ultrapure water, 1 mL of Ab_2 (10 μg mL^{-1}) was added to the suspension, which was then oscillated for 5 h at 4 °C. Afterwards, 500 μL (0.1 %) of BSA was added to the above solution, which was incubated for 1 h. Then the solution was centrifuged and filtered in refrigerated centrifuge to obtain the precipitate. Finally, the obtained precipitate was dispersed into 3 mL of PBS (pH = 7.4) solution, which was placed in the refrigerator at 4 °C.

2.5. Preparation and detection procedure of the biosensor

The specific construction process of the PEC biosensor is shown in Scheme 1. Firstly, FTO glass sheets measuring 4 cm by 2 cm covered by the photoelectricity materials were cut into smaller glass sheets

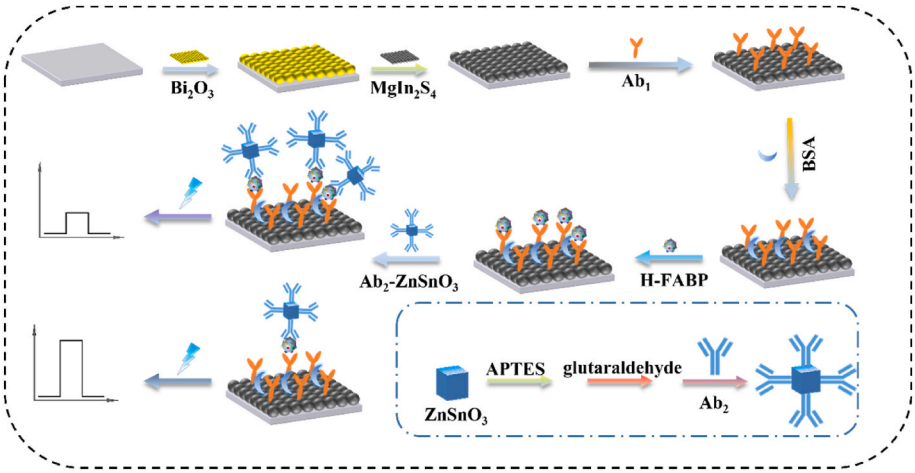

Scheme 1. Preparation Process of Photoelectrochemical Biosensor.

measuring 2 cm by 1 cm with material area of 0.6 cm^2. Then, 6 μL of TGA (3 mM) was added dropwise on the FTO glass sheets surface and incubated for 40 min to obtain the TGA/$MgIn_2S_4$/Bi_2O_3/FTO electrode. Afterwards, 10 μL of EDC/NHS (15 mg mL^{-1} NHS and 30 mg mL^{-1} EDC), Ab_1, BSA, Ag and Ab_2-$ZnSnO_3$ were hatched in sequence at room temperature for 1 h each time to gain a $ZnSnO_3$/Ab_2/Ag/BSA/Ab_1/TGA/$MgIn_2S_4$/Bi_2O_3/FTO photoelectrode.

Photocurrent tests were carried out using the prepared photoelectrode as the working electrode, saturated calomel electrode as the reference electrode, platinum electrode as the counter electrode and PBS as the electrolyte solution.

3. Results and discussion

3.1. Characterization of materials Bi_2O_3, $Bi_2O_3/MgIn_2S_4$, $ZnSnO_3$

The composition and microstructure of materials Bi_2O_3, Bi_2O_3/$MgIn_2S_4$ and $ZnSnO_3$ were characterized using physical characterization techniques such as Scanning electron microscopy (SEM), X-ray diffraction (XRD) and Transmission electron microscopy (TEM). Fig. 1A

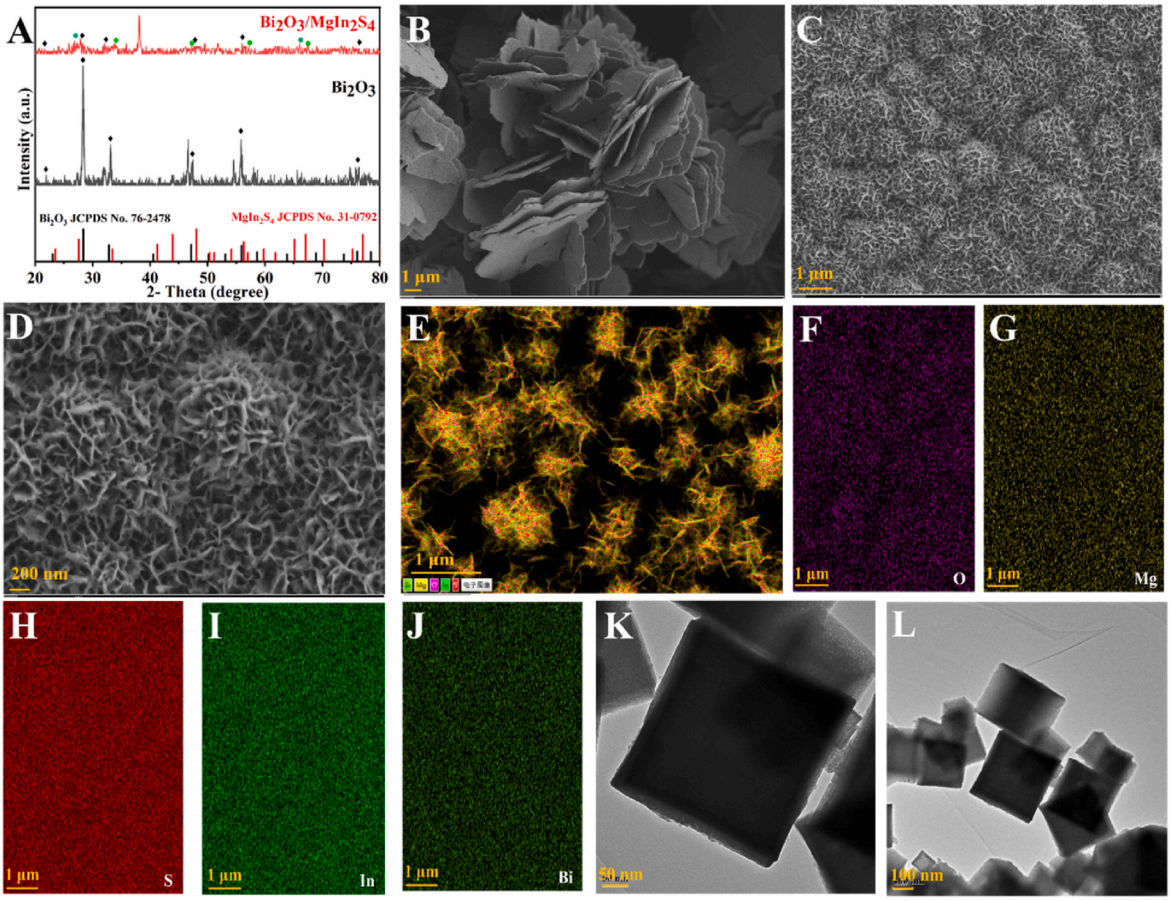

Fig. 1. (A) XRD patterns of Bi_2O_3, Bi_2O_3/$MgIn_2S_4$, (B) SEM image of Bi_2O_3, (C, D) SEM image of Bi_2O_3/$MgIn_2S_4$, (E), (F), (G), (H), (I) and (J) mapping images of O, Mg, S, In and Bi elements, (K, L) TEM images of $ZnSnO_3$.

displays the XRD patterns of Bi_2O_3 and $Bi_2O_3/MgIn_2S_4$. The diffraction peaks of Bi_2O_3 are consistent with the XRD patterns provided by the reference, which are matched with the reference (JCPDS, PDF #76–2478) at 23.060° (1 1 0), 28.340° (1 1 1), 32.839° (2 0 0), 47.126° (2 2 0), 55.907° (3 1 1), 76.059° (3 3 1). In addition, the XRD pattern of the synthetized $Bi_2O_3/MgIn_2S_4$ heterojunction material at 27.062° (3 1 1), 33.445° (4 0 0), 48.022° (4 4 0), 56.289° (5 3 3), 65.133° (6 4 2), 67.087° (7 3 1) is matched with the diffraction peaks of $MgIn_2S_4$ (JCPDS, PDF #31–0792). The positions of the diffraction peaks of both Bi_2O_3 and $MgIn_2S_4$ in the heterojunction material are consistent with the positions of the diffraction peaks in the PDF standard card, providing strong evidence of the successful synthesis of the composite material. Furthermore, the XRD pattern that is exhibited in Fig. S1 demonstrates the successful preparation of $ZnSnO_3$, which is same to the reference. In Fig. S1, only one broad diffraction peak of the FTO glass sheet is present, indicating that the synthetized $ZnSnO_3$ material is amorphous at this temperature, as explained in reference.

SEM images of Bi_2O_3 and $Bi_2O_3/MgIn_2S_4$ exhibited in Fig. 1B, C,D were used to demonstrate the micro-morphological information. In comparison with densely grown Bi_2O_3 nanosheets (Fig. 1B), it was clear that the surface of Bi_2O_3 was covered with $MgIn_2S_4$ nanosheets that were much smaller in size than Bi_2O_3 nanosheets (Fig. 1C and D), which formed a structure that was similar to flower, and the presence of the elements O, Mg, S, In and Bi were demonstrated by elemental mapping in Fig. 1F, G, H, I and J. Fig. 1K and L displayed the TEM image of $ZnSnO_3$ which was examined to gather information on its morphology. As shown in the figure, the cubic $ZnSnO_3$ material was successfully prepared, and the size of the material was about 300 nm, and its homogeneous and dispersed state provided the basis for labeling the second antibody.

According to the display of Fig. 2 and Fig. S2, further evidence was provided through X-ray Photoelectron Spectroscopy (XPS) analysis, confirming the presence of $Bi_2O_3/MgIn_2S_4$ and $ZnSnO_3$. The XPS spectra that is exhibited in Fig. 2B displays two strong peaks at 163.6 eV and 158.3 eV, corresponding to Bi $4f_{5/2}$ and Bi $4f_{7/2}$, which is matched well with the standard Bi^{3+} peaks in Bi_2O_3. The peaks at 161.0 eV and 162.1 eV correspond to the S 2p transition, belonging to the binding energy of S^{2-}. The O 1s spectrum (Fig. 2A) contains two peaks that can be ascribed to oxygen vacancy (532.1 eV) and lattice oxygen (530.6 eV). The high-resolution XPS spectra shows a peak at 1304 eV in Fig. 2D, belonging to Mg 1s, which corresponds to Mg^{2+} in the $MgIn_2S_4$ material. As shown in Fig. 2C, the two peaks shown in the high-resolution spectra at 452.3 and 444.7 eV are matched with the two binding energies of In $3d_{3/2}$ and In $3d_{5/2}$, which are attributed to In^{3+} in the $MgIn_2S_4$ material. The successful preparation of $ZnSnO_3$ was further verified using X-ray photoelectron spectroscopy (XPS), where O, Zn and Sn elements were all perfectly represented that are shown in Fig. S3. The peaks of O 1s, Zn 2p and Sn 3d shown in the figure were in good agreement with reference.

3.2. Possible mechanisms of PEC detection

The UV–vis diffuse reflectance spectra of Bi_2O_3, $MgIn_2S_4$ and $ZnSnO_3$ are exhibited in Fig. S4 in order to determine the band gap of synthetized materials. The absorption edge of Bi_2O_3 and the $MgIn_2S_4$ nanoparticles that were measured by experiment corresponded to the band gap energies of 2.7 eV and 2.07 eV, respectively. The band gap of $ZnSnO_3$ nanomaterial that was measured by UV–vis diffuse reflectance spectra was determined to be 3.42 eV.

In addition, the band structures of Bi_2O_3 and $MgIn_2S_4$ have been determined by means of Mott-Schottky curves. As can be seen in Fig. S5, the lines have the positive slope, which indicate that these semiconductor materials are n-type semiconductors. The flat band potential (E_{fb}) for Bi_2O_3 is 0.09 V vs. SCE, corresponding to 0.33 V vs. NHE, while for $MgIn_2S_4$ it is −0.98 V vs. SCE, which corresponds to −0.74 V vs. NHE. Based on the reported literature, the conduction band potential of n-type semiconductors is negative 0.1–0.3 V compared to flat band potential of n-type semiconductors. Thus, the conduction band potential (E_{CB}) of Bi_2O_3 and $MgIn_2S_4$ are 0.23 V vs. NHE and −0.84 V vs. NHE. Furthermore, the valence band potentials (E_{VB}) of Bi_2O_3 and $MgIn_2S_4$ were calculated to be +2.93 V and +1.23 V by using the conduction

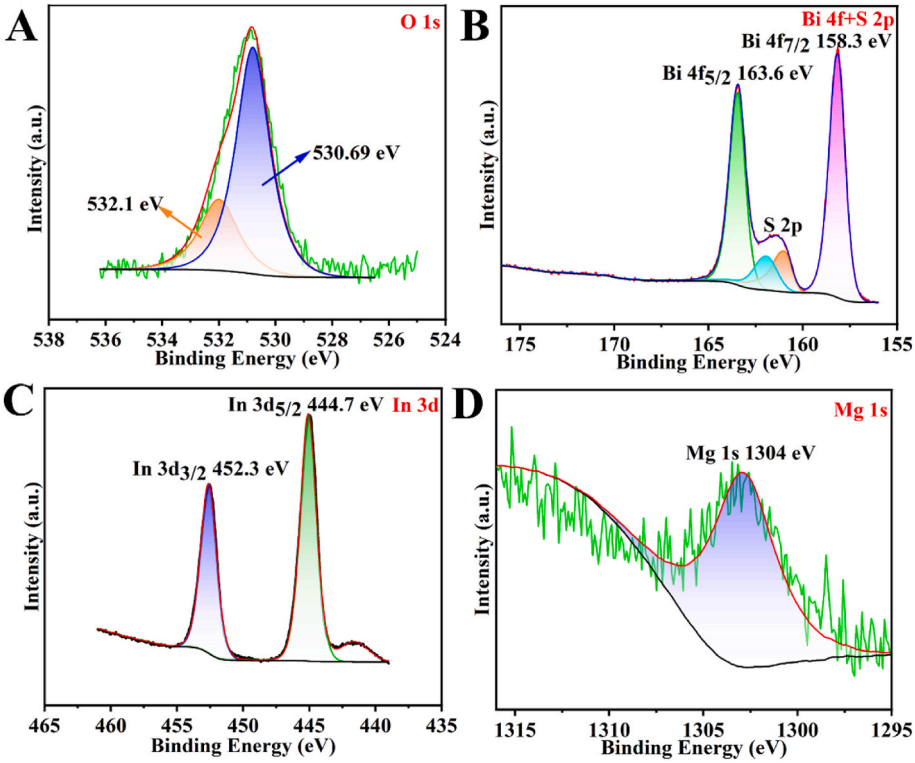

Fig. 2. XPS spectra of (A) O 1s, (B) Bi 4f and S 2p, (C) In 3d, (D) Mg 1s.

band potentials (E_{CB}), band gaps (E_g) and the corresponding equation. The potentials of both the valence and conduction bands of Bi_2O_3 are higher than those of $MgIn_2S_4$, which constitutes a typical type-II heterojunction.

Thus, Bi_2O_3 and $MgIn_2S_4$ semiconductor materials form a typical type-II heterojunction, which accelerates the separation of photogenerated electrons and holes, resulting in enhanced photocurrent signal. The electron transfer mechanism of the prepared photoelectrochemical biosensor is exhibited in Fig. 3A. Under the influence of excitation light source, electrons in the valence band of Bi_2O_3 and $MgIn_2S_4$ absorbed photon energy and were excited to jump to the conduction band. Since the VB and CB of Bi_2O_3 were perfectly matched with those of $MgIn_2S_4$, the photogenerated electrons in the CB of $MgIn_2S_4$ can migrate into the CB of Bi_2O_3. Finally, the electrons in the CB of Bi_2O_3 were migrated into the FTO electrode, resulting in the photocurrent signal response. The photogenerated holes of Bi_2O_3 simultaneously migrate towards the VB of $MgIn_2S_4$ and then are trapped by ascorbic acid in electrolyte, which greatly inhibits the complexation of photogenerated carriers and results in a greatly improved photocurrent response. However, as $ZnSnO_3$ is gradually captured, $ZnSnO_3$ absorbs part of the visible light (Fig. S4D) while the steric hindrance of $ZnSnO_3$ hinders the electron transfer between ascorbic acid and photoelectrode. Under the dual effect, the photocurrent response gradually decreases as the concentration of H-FABP rises.

3.3. Characterization of the biosensor

Electrochemical impedance spectroscopy (EIS) obtained by using 5 mV sine wave potential as jamming signal was used to characterize the successful preparation of PEC biosensor. In Fig. 3B, it can be seen that the electron transfer resistance is relatively lower when only the bare FTO photoelectrode is present, and the electron transfer resistance gradually increases as the materials are modified layer by layer onto the photoelectrode. Since the primary antibody, antigen, and secondary antibody linking to the marker modified to the photoelectrode are non-conducting proteins, the electron transfer resistance obtained a significant increase when they were modified to the photoelectrode, which indicates the successful preparation of the photoelectrode.

PEC response (Fig. 3C) was used to validate the successful construction of the PEC biosensor. FTO has no photocurrent under the excitation of visible light. Due to the well-matched band structures, the PEC response of the type-II heterojunction $Bi_2O_3/MgIn_2S_4$ was much higher than that of bare Bi_2O_3. Subsequently, after immobilization of the primary antibody, BSA, and the secondary antibody, the photocurrent gradually decreased which suppressed the electron transfer due to the increased spatial site resistance. At the same time, the marker with the attached secondary antibody also absorbs some of the visible light, which can lead to a further decrease in photocurrent.

3.4. Optimization of experimental conditions

To obtain the best performance of the PEC biosensor, the experimental conditions such as the concentration of ascorbic acid and pH were screened to find the optimal factors.

The influence of various concentrations of ascorbic acid on the photocurrent signal is demonstrated in Fig. 4A. It is thus clear that the photocurrent increases gradually as the concentration of ascorbic acid increases from 0.04 mol L^{-1} to 0.1 mol L^{-1} and reaches a maximum at a concentration of 0.1 mol L^{-1}, after which it gradually decreases. Therefore, 0.1 mol L^{-1} of ascorbic acid is the optimal concentration. When the pH of the PBS is 7.4, the photocurrent intensity is highest, which is chosen as the electrolyte solution for the biosensor (Fig. 4B).

3.5. H-FABP analysis

On the basis of the best-of-breed experimental factors, immunoassay performance was measured for H-FABP that the concentration ranges from 0.05 pg/mL to 100 ng/mL. A calibrated operating curve (Fig. 5B) was obtained by plotting the logarithm of the concentration of H-FABP as the horizontal coordinate and the photocurrent signal as the vertical coordinate. The functional equation was I = −15.69 lgc+87.14 and the detection limit calculated from the equation of the biosensor was 0.029 pg/mL. When comparing biosensor outlined in this study with previously reported methods, it was clear that the work has a significant advantage in both detection range and limit.

3.6. Analysis of the biosensor performance

The reproducibility and selectivity of biosensor are significant measures of the performance of the sensor. Thus, to investigate the selectivity of the prepared biosensor, NT-pro BNP (neuronal precursor brain natriuretic peptide), NSE (neuro-specific enolase) and cTnI (cardiac troponin I) were chosen as experimental disrupters. As suggested in Fig. 5C–as the experimental disrupters were gauged alone, the photocurrent response was similar to the photoelectrode with merely semiconductor heterojunction material, Ab_1 and BSA attached. When experimental disrupters were placed in the solution including the antigen (H-FABP), the relative standard deviations (RSD) of the results were calculated and obtained to be 2.05 % and 2.08 %, which indicated good selectivity of the prepared biosensor. Additionally, as a test for the reproducibility of the PEC sensor (Fig. 5D), five electrodes were prepared under the same experimental requirements for the detection of H-FABP (c = 0.1 ng/ml). The data was exhibited in Fig. 5D and the relative standard deviation (RSD) value was 2.07 % suggesting that the synthetized biosensor had great reproducibility.

3.7. Real sample analysis

The recovery of H-FABP in real samples was assayed using the

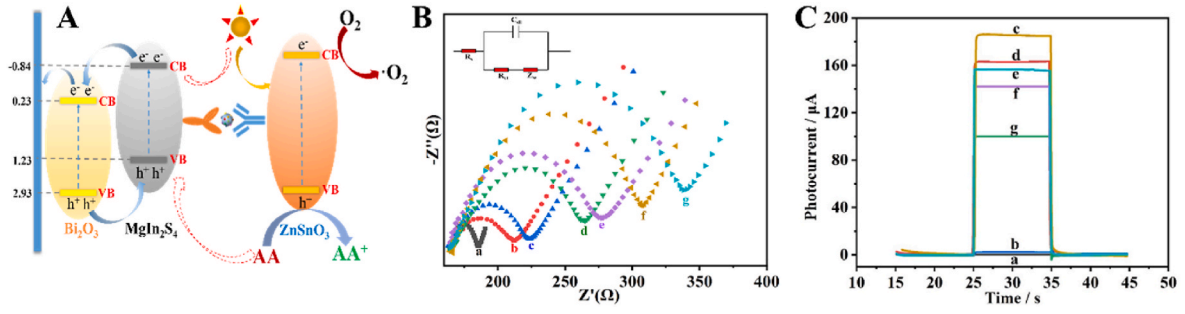

Fig. 3. (A)mechanism of PEC, (B) PEC signal of (a) FTO, (b) FTO/Bi_2O_3, (c) FTO/Bi_2O_3/$MgIn_2S_4$, (d) FTO/Bi_2O_3/$MgIn_2S_4$/Ab_1, (e) FTO/Bi_2O_3/$MgIn_2S_4$/Ab_1/BSA, (f) FTO/Bi_2O_3/$MgIn_2S_4$/Ab_1/BSA/Ag ($C_{H\text{-}FABP}$ = 0.1 ng/mL), (g) FTO/Bi_2O_3/$MgIn_2S_4$/Ab_1/BSA/Ag/Ab_2/$ZnSnO_3$ (C) EIS of the layer modification process ($C_{H\text{-}FABP}$ = 0.1 ng/mL).

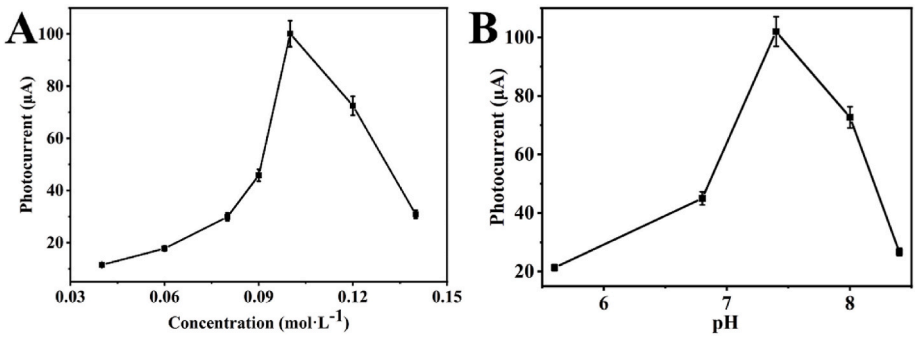

Fig. 4. (A) The concentration of ascorbic acid ($C_{H\text{-}FABP}$ = 0.1 ng/mL), (B) The pH of PBS ($C_{H\text{-}FABP}$ = 0.1 ng/mL).

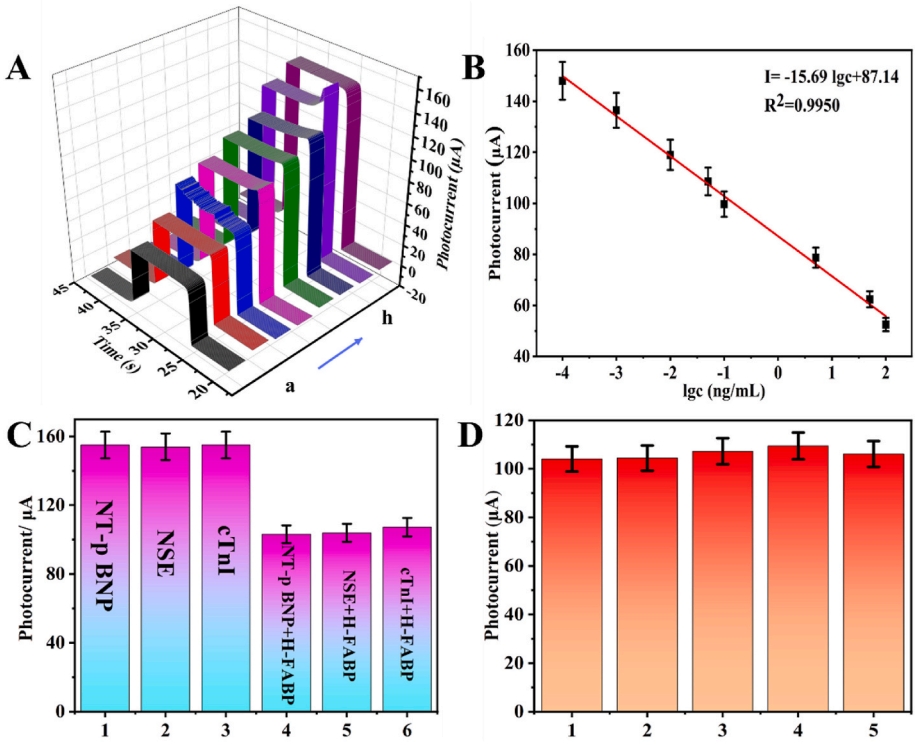

Fig. 5. (A) Photocurrent signal response, (B) The calibrated operating curve of H-FABP test: (a–h): 100, 50, 5, 0.1, 0.05, 0.01, 0.001, 0.00005 ng mL^{-1}, (C) Selectivity ($C_{H\text{-}FABP}$ = 0.1 ng/mL), (D) Reproducibility ($C_{H\text{-}FABP}$ = 0.1 ng/mL). Error bars = SD (n = 3).

standard addition method with the aim of validating the feasibility and usefulness of prepared biosensor for pathological detection. By adding varying degrees of concentration of H-FABP to pre-treated human serum diluted 10 times, the results obtained from the experiment indicate that the recovery rate range was between 90.9 % and 104.6 %, with RSD values ranging from 2.2 % to 4.3 %. The above results that were shown in Table S1 make known that synthetized biosensor has promising applications in clinical testing.

4. Conclusion

In the work, a high-performance photoelectrochemical biosensor for ultra-sensitive detection of H-FABP is fabricated with $Bi_2O_3/MgIn_2S_4$ heterojunction as photoelectronic material and $ZnSnO_3$ as the effective quencher. The innovatively synthetized Bi_2O_3 and $MgIn_2S_4$ materials based on in-situ generation method forms a type-II heterojunction, which inhibits the complexation of photogenerated carriers and facilitates the transfer of electrons. Due to the extremely well-matched energy band positions of Bi_2O_3 and $MgIn_2S_4$, the initial photocurrent signal response is exceptionally high. Moreover, cubic $ZnSnO_3$ synthetized by hydrothermal method is used as the excellent quencher, which not only competes with the substrate material for visible light but also hinders the reaction of ascorbic acid with the substrate material through steric hindrance effect, resulting in a significant reduction in the photocurrent signal response. Thus, photoelectrochemical biosensor with high sensitivity is successfully prepared based on a dual quenching strategy, providing higher accuracy and efficiency in the early detection of disease.

CRediT authorship contribution statement

Haiyang Gao: Writing – original draft, Data curation, Conceptualization. **Xuan Kuang:** Funding acquisition. **Bing An:** Data curation. **Jinjie Liu:** Data curation. **Kun Xu:** Methodology. **Hongmin Ma:** Methodology. **Dongquan Leng:** Writing – review & editing, Methodology. **Xuejing Liu:** Funding acquisition. **Qin Wei:** Project administration, Funding acquisition. **Huangxian Ju:** Writing – review & editing, Funding acquisition.

Declaration of competing interest

The authors declare that they have no known competing financial interests or personal relationships that could have appeared to influence the work reported in this paper.

Data availability

The authors do not have permission to share data.

Acknowledgements

This study was supported by the National Natural Science Foundation of China (No.22274062, 22206056), the Shandong Provincial Natural Science Foundation (No. ZR2022QB117), Special Foundation for Taishan Scholar Professorship of Shandong Province. The authors thanks Shiyanjia Lab (www.shiyanjia.com) for XPS analysis.

Appendix A. Supplementary data

Supplementary data to this article can be found online at https://doi.org/10.1016/j.talanta.2024.126272.

References

[1] Y. Gao, Y. Zeng, X. Liu, D. Tang, Liposome-Mediated in situ formation of type-I heterojunction for amplified photoelectrochemical immunoassay, Anal. Chem. 94 (11) (2022) 4859–4865.
[2] L. Gao, Y. Zhou, L. Cao, X. Cui, Y. Zheng, H. Yin, S. Ai, Photoelectrochemical biosensor for Histone deacetylase Sirt1 detection based on polyaspartic acid-engaged and triggered redox cycling amplification and enhanced photoactivity of $BiVO_4$ by gold nanoparticles and SnS_2, Anal. Chem. 94 (48) (2022) 16936–16944.
[3] M. Chen, J. Guo, F. Mo, W. Yu, Y. Fu, Highly sensitive photoelectrochemical immunosensor based on organic multielectron donor nanocomposite as signal probe, Anal. Chem. 94 (49) (2022) 17039–17045.
[4] C. Mao, L. Wu, Y. Wen, X. Tang, Z. Huang, L. Zhao, Photoelectrochemical immunosensor for carcinoembryonic antigen detection-an attempt for early cancer screening, Biosens. Bioelectron. 220 (2023).
[5] M. Hu, J. Wang, J. Han, Y. Rong, H. Yu, S. Ge, H. Yang, L. Zhang, J. Yu, Nuclease-propelled target dual-recycling amplification strategy integrated with cascaded sensitization effect of $ZnO/CuInS_2/Ag_2Se$ photoactive structures for lab-on-paper photoelectrochemical microRNA bioassay, Sensor. Actuator. B Chem. 369 (2022).
[6] Y.-Z. Shen, J. Guan, C. Ma, Y. Shu, Q. Xu, X.-Y. Hu, Competitive displacement triggering DBP photoelectrochemical aptasensor via cetyltrimethylammonium bromide bridging aptamer and perovskite, Anal. Chem. 94 (3) (2022) 1742–1751.
[7] Y. Zhou, H. Yin, S. Ai, Recent advances and applications of Bi_2S_3-based composites in photoelectrochemical sensors and biosensors, TrAC, Trends Anal. Chem. 158 (2023).
[8] X. Wang, X. Rong, Y. Zhang, F. Luo, B. Qiu, J. Wang, Z. Lin, Homogeneous photoelectrochemical aptasensors for tetracycline based on sulfur-doped g-C_3N_4/n-GaN heterostructures formed through self-assembly, Anal. Chem. 94 (8) (2022) 3735–3742.
[9] T. Wu, Y. Du, Z. Gao, K. Xu, L. Dai, L. Liu, F. Li, Q. Wei, H. Ju, Dual direct Z-scheme heterojunction with stable electron supply to a Au/PANI photocathode for ultrasensitive photoelectrochemical and electrochromic visualization detection of ofloxacin in a microfluidic sensing platform, Anal. Chem. (2022).
[10] Y. Zhou, H. Yin, S. Ai, Applications of two-dimensional layered nanomaterials in photoelectrochemical sensors: a comprehensive review, Coord. Chem. Rev. 447 (2021).
[11] T. Wu, Y. Du, L. Dai, J. Li, X. Song, J. Feng, X. Wang, Q. Wei, H. Ju, A direct Z-scheme AgBr/$CuBi_2O_4$ photocathode for ultrasensitive detection of ciprofloxacin and ofloxacin by controlling the release of luminol in self-powered microfluidic photoelectrochemical aptasensors, Anal. Chem. 94 (30) (2022) 10651–10658.
[12] Y.-Y. Wei, S.-H. Wu, Q.-M. Wang, J.-J. Sun, A novel split-type photoelectrochemical biosensor based on double-strand specific nuclease-assisted cycle amplification coupled with plasmonic Ag enhanced $BiVO_4$ performance for sensitive detection of microRNA-155, Sensor. Actuator. B Chem. 369 (2022).
[13] L. Yang, X. Liu, L. Li, S. Zhang, H. Zheng, Y. Tang, H. Ju, A visible light photoelectrochemical sandwich aptasensor for adenosine triphosphate based on $MgIn_2S_4$-TiO_2 nanoarray heterojunction, Biosens. Bioelectron. 142 (2019).
[14] D. Long, Y. Tu, Y. Chai, R. Yuan, Photoelectrochemical assay based on SnO_2/BiOBr p–n heterojunction for ultrasensitive DNA detection, Anal. Chem. 93 (38) (2021) 12995–13000.
[15] J. Wang, J. Xie, M. Chen, S. Zheng, H. Tan, S. Yu, Y. Chen, X. Huang, W. Gao, Core-double-shell structure and heterojunction in CdS/SnS_2 boosting fast carrier separation for ultrasensitive detection of carbohydrate antigen 125, Sensor. Actuator. B Chem. 380 (2023).
[16] J. Xu, R. Zeng, L. Huang, Z. Qiu, D. Tang, Dual-signaling photoelectrochemical biosensor based on biocatalysis-induced vulcanization of Bi_2MoO_6 nanosheets, Anal. Chem. 94 (32) (2022) 11441–11448.
[17] T. Wu, X. Song, X. Ren, L. Dai, H. Ma, D. Wu, Y. Li, Q. Wei, H. Ju, Catalytic decomposition of the hole-derived H2O2 by $AgBiS_2$@Ag nanozyme to enhance the photocurrent of Z-scheme $BiVO_4/ZnIn_2S_4$ photoelectrode in microfluidic immunosensing platform, Anal. Chem. 94 (35) (2022) 12127–12135.
[18] J. Zhang, X. Wang, M. Liang, M. Han, J. Dai, Q. Wei, T.Z. Oo, S.H. Aung, K.N. Hui, F. Chen, High-performance photoelectrochemical desalination based on the dye-sensitized Bi_2O_3 anode, ACS Appl. Mater. Interfaces 14 (29) (2022) 33024–33031.
[19] D.-N. Chen, G.-Q. Wang, L.-P. Mei, J.-J. Feng, A.-J. Wang, Dual II-scheme nanosheet-like $Bi_2S_3/Bi_2O_3/Ag_2S$ heterostructures for ultrasensitive PEC aptasensing of aflatoxin B1 coupled with catalytic signal amplification by dendritic nanorod-like Au@Pd@Pt nanozyme, Biosens. Bioelectron. 223 (2023).
[20] X. Chen, W. Wu, Q. Zhang, C. Wang, Y. Fan, H. Wu, Z. Zhang, Z-scheme Bi_2O_3/$CuBi_2O_4$ heterojunction enabled sensitive photoelectrochemical detection of aflatoxin B1 for health care, the environment, and food, Biosens. Bioelectron. 214 (2022).
[21] Y. Li, J. Zhong, J. Li, S. Huang, S. Zhang, H. Yang, L. Ma, Enhanced visible light-driven photocatalytic destruction of decontaminants over $Bi_2O_3/BiVO_4$ heterojunctions with rich oxygen vacancies, Chem. Phys. Lett. 801 (2022).
[22] S.-Y. Yu, L. Zhang, L.-B. Zhu, Y. Gao, G.-C. Fan, D.-M. Han, G. Chen, W.-W. Zhao, Bismuth-containing semiconductors for photoelectrochemical sensing and biosensing, Coord. Chem. Rev. 393 (2019) 9–20.
[23] J. Tang, T. Zhang, Q. Zhang, Z. Duan, C. Li, D. Hou, Q. Xv, C. Meng, Y. Zhang, Y. Zhu, In-situ growth UiO-66 on Bi_2O_3 to fabrication p-p heterojunction with enhanced visible-light degradation of tetracycline, J. Solid State Chem. 302 (2021).
[24] Y.-C. Liang, Y.-H. Chou, Improved photoelectrode performance of chemical solution-derived Bi2O3 crystals via manipulation of crystal characterization, RSC Adv. 10 (73) (2020) 45042–45058.
[25] Y. Lee, M. Cui, J. Choi, J. Kim, Y. Son, J. Khim, Degradation of polychlorinated dibenzo-p-dioxins and dibenzofurans in real-field soil by an integrated visible-light photocatalysis and solvent migration system with p-n heterojunction $BiVO_4/Bi_2O_3$, J. Hazard Mater. 344 (2018) 1116–1125.
[26] X. Yan, R. Pu, R. Xie, B. Zhang, Y. Shi, W. Liu, G. Ma, N. Yang, Design and fabrication of $Bi_2O_3/BiFeO_3$ heterojunction film with improved photoelectrochemical performance, Appl. Surf. Sci. 552 (2021).
[27] Y. Wang, H. Yin, X. Li, G.I.N. Waterhouse, S. Ai, Photoelectrochemical immunosensor for N6-methyladenine detection based on Ru@UiO-66, Bi_2O_3 and Black TiO_2, Biosens. Bioelectron. 131 (2019) 163–170.
[28] F.X. Wang, C. Ye, S. Mo, H.Q. Luo, J.R. Chen, Y. Shi, N.B. Li, Enhanced photoelectrochemical sensing based on novel synthesized Bi_2S_3@Bi_2O_3 nanosheet heterostructure for ultrasensitive determination of l-cysteine, Anal. Bioanal. Chem. 411 (14) (2019) 3059–3068.
[29] I. Khan, A. Abdalla, A. Qurashi, Synthesis of hierarchical WO_3 and Bi_2O_3/WO_3 nanocomposite for solar-driven water splitting applications, Int. J. Hydrogen Energy 42 (5) (2017) 3431–3439.
[30] T. Ke, S. Shen, K. Yang, D. Lin, In situ fabrication of $Bi_2O_3/C_3N_4/TiO_2$@C photocatalysts for visible-light photodegradation of sulfamethoxazole in water, Appl. Surf. Sci. 580 (2022).
[31] L. Biswal, L. Acharya, B.P. Mishra, S. Das, G. Swain, K. Parida, Interfacial solid-state mediator-based Z-scheme heterojunction TiO_2@$Ti_3C_2/MgIn_2S_4$ microflower for efficient photocatalytic pharmaceutical micropollutant degradation and hydrogen generation: stability, kinetics, and mechanistic insights, ACS Appl. Energy Mater. 6 (3) (2023) 2081–2096.
[32] G. Swain, S. Sultana, K. Parida, Constructing a novel surfactant-free MoS2 nanosheet modified $MgIn_2S_4$ marigold microflower: an efficient visible-light driven 2D-2D p-n heterojunction photocatalyst toward HER and pH regulated NRR, ACS Sustain. Chem. Eng. 8 (12) (2020) 4848–4862.
[33] H. Yin, T. Fan, Y. Cao, P. Li, X. Yao, X. Liu, Construction of three-dimensional MgIn2S4 nanoflowers/two-dimensional oxygen-doped g-C_3N_4 nanosheets direct Z-scheme heterojunctions for efficient Cr(VI) reduction: insight into the role of superoxide radicals, J. Hazard Mater. 420 (2021).
[34] J. Huang, X. Xu, C. Gu, W. Wang, B. Geng, Y. Sun, J. Liu, Size-controlled synthesis of porous $ZnSnO_3$ cubes and their gas-sensing and photocatalysis properties, Sensor. Actuator. B Chem. 171–172 (2012) 572–579.
[35] C. Tuc Altaf, N.S. Sahsuvar, N. Abdullayeva, O. Coskun, A. Kumtepe, E. Karagoz, M. Sankir, N. Demirci Sankir, Inverted configuration of Cu(in,Ga)S_2/in_2S_3 on 3D-ZnO/$ZnSnO_3$ bilayer system for highly efficient photoelectrochemical water splitting, ACS Sustain. Chem. Eng. 8 (40) (2020) 15209–15222.
[36] M. Li, S. An, Y. Wu, Z. Yan, Y. Chai, R. Yuan, Self-supplied electron photoelectrochemical biosensor with PTB7-Th as a photoelectric material and biotin as an efficient quencher, ACS Appl. Mater. Interfaces 14 (47) (2022) 53398–53404.
[37] M. Lv, C. Zong, X. Chen, X. Lin, L. Kong, C. Li, A cathodic photoelectrochemical biosensor based on CRISPR/Cas12a trans-cleavage mediated p-n heterojunction quenching mode for microRNA determination, Anal. Chim. Acta 1268 (2023).
[38] L. Meng, K. Xiao, X. Zhang, C. Du, J. Chen, A novel signal-off photoelectrochemical biosensor for M.SssI MTase activity assay based on GQDs@ZIF-8 polyhedra as signal quencher, Biosens. Bioelectron. 150 (2020).
[39] C.-Q. Zhao, J. Zhou, K.-W. Wu, S.-N. Ding, J.-J. Xu, H.-Y. Chen, Plasmonic enhanced gold nanoclusters-based photoelectrochemical biosensor for sensitive alkaline phosphatase activity analysis, Anal. Chem. 92 (10) (2020) 6886–6892.
[40] D. Leng, R. Xu, X. Ren, H. Ma, L. Liu, Q. Wei, H. Ju, Self-shedding of multifunctional biomolecular nanocarriers for H-FABP monitoring in magnetic

separation self-powered photoelectrochemical and colorimetric immunoassay platform, Chem. Eng. J. 469 (2023).
[41] J. Shu, D. Tang, Recent advances in photoelectrochemical sensing: from engineered photoactive materials to sensing devices and detection modes, Anal. Chem. 92 (1) (2019) 363–377.
[42] H. Li, J. Zhao, T. Wu, Z. Fu, W. Zhang, Z. Lian, S. Cai, R. Yang, Dual ligand-induced photoelectrochemical sensing by integrating Pt/MoS_2 heterostructure and Au polyhedra for sensitive detection of SARS-CoV-2, Sensor. Actuator. B Chem. 376 (2023).
[43] Y. Du, S. Yu, Z. Li, H. Ju, Photocurrent quenching by competitive consumption of surface electron donor and light absorption for immunosensing, Anal. Chim. Acta 1221 (2022).